Global M_2 internal tide and its seasonal variability from high resolution ocean circulation and tide modeling

M. Müller,[1] J. Y. Cherniawsky,[2] M. G. G. Foreman,[2] and J.-S. von Storch[3]

[1] The present study describes a model simulation, where ocean tide dynamics are simulated simultaneously with the ocean circulation. The model is forced by a lunisolar tidal forcing described by ephemerides and by daily climatological wind stress, heat, and fresh water fluxes. The horizontal resolution is about $0.1°$ and thus, the model implicitly resolves meso-scale eddies and internal waves. In this model simulation the global M_2 barotropic to baroclinic tidal energy conversion amounts to 1.2 TW. We show global maps of the surface signature of the M_2 baroclinic tide and compare it with an estimate obtained from 19 years of satellite altimeter data. Further, the simulated seasonality in the low mode internal tide field is presented and, as an example, the physical mechanisms causing the non-stationarity of the internal tide generated in Luzon Strait are discussed. In general, this study reveals the impact of inter-annual changes of the solar radiative forcing and wind forced ocean circulation on the generation and propagation of the low mode internal tides. The model is able to simulate non-stationary signals in the internal tide field on global scales which have important implications for future satellite altimeter missions. **Citation:** Müller, M., J. Y. Cherniawsky, M. G. G. Foreman, and J.-S. von Storch (2012), Global M_2 internal tide and its seasonal variability from high resolution ocean circulation and tide modeling, *Geophys. Res. Lett.*, *39*, L19607, doi:10.1029/2012GL053320.

1. Introduction

[2] In the last two decades satellite altimetry has enabled global mapping of the barotropic and low mode baroclinic tides with a constantly increasing accuracy [*Ray and Mitchum*, 1997; *Ray and Zaron*, 2011]. The highly advanced geodetic monitoring system and the sharp tidal peaks enable such observations from space with an accuracy of O(5 mm). The surface signature of the internal tides amounts to only 5–30 mm, whereas below the surface, in deeper ocean regions the corresponding wave amplitudes are much higher, of O(10–100 m), which makes them of considerable importance for the understanding of mixing processes.

[3] Apart from their importance for deep ocean mixing and, in turn, ocean circulation, the increasing accuracy of geodetic measurements demands highly accurate barotropic, and for future satellite missions, baroclinic ocean tide models in order to correct the geodetic time series for aliasing errors. The accuracy of the simulation of barotropic tides has improved significantly in the last decades by using ocean tide models constrained by satellite altimeter data and has approached an accuracy of a few centimeters for deep ocean tides [*Shum et al.*, 1997]. Barotropic ocean tide model simulations without data constraints are less accurate, but they are still able to capture more than 90% of the tidal sea surface variability [*Arbic et al.*, 2004; *Griffiths and Peltier*, 2009].

[4] Global simulations of baroclinic tides in layered baroclinic tide models have been obtained by *Simmons et al.* [2004] and *Arbic et al.* [2004], whereas a first simulation of baroclinic tides in a realistic global ocean circulation model has been performed by *Arbic et al.* [2010]. The latter shows a good accuracy of the barotropic tide patterns and even presents realistic magnitudes and phases of the sea surface signature of internal waves [see also *Arbic et al.*, 2012].

[5] In the present study we introduce a global high resolution ocean tide and circulation model with an embedded thermodynamic sea-ice model, which is explicitly forced by the full lunisolar tidal forcing of second degree as described by ephemerides [*Bretagnon and Francou*, 1988; *Thomas et al.*, 2001]. A striking result from a 10-year long simulation is, that the barotropic and low mode baroclinic tides are well captured, and allow us to compute and examine the seasonality of the internal tide field. This study shows model results complementary to a recently published analysis of satellite altimeter data on the stationarity of the internal tides [*Ray and Zaron*, 2011]. Studies on these processes have important consequences for planned future satellite altimeter missions.

2. Ocean Model Description

[6] The general ocean circulation model is the Max Planck Institute - Ocean Model (MPI-OM) with an embedded thermodynamic sea-ice model [*Jungclaus et al.*, 2006]. The model grid is represented vertically by 40 z-layers, where nine layers are in the upper 100 meter of the ocean. The horizontal grid is a tripolar spherical grid with an almost uniform resolution of $0.1°$, and thus grid sizes are generally about 10 km and become smaller in high latitudes. This high-resolution ocean model approach has been developed within the framework of the German consortium project STORM, where a high-resolution coupled climate simulation is in preparation.

[7] The model is forced by climatological wind forcing. Sea surface temperature and salinity are restored to monthly climatological values [*Steele et al.*, 2001], in order to maintain a stationary mixed layer depth. The restoring is adjusted to prevent phase and amplitude changes of the modeled seasonal cycle [*Cherniawsky and Holloway*, 1991]. The

---

[1]School of Earth and Ocean Sciences, University of Victoria, Victoria, British Columbia, Canada.
[2]Institute of Ocean Sciences, Fisheries and Oceans Canada, Sidney, British Columbia, Canada.
[3]Max-Planck Institute for Meteorology, Hamburg, Germany.

Corresponding author: M. Müller, School of Earth and Ocean Sciences, University of Victoria, PO Box 1700 STN CSC, Victoria, BC V8W 2Y2, Canada. (mmueller@uvic.ca)

(a)

(b)
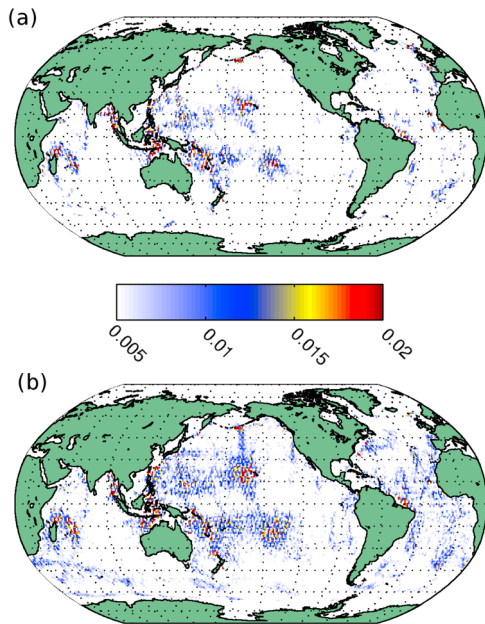
Figure 1. RMS amplitudes (in meter) of the M_2 internal tide surface signature (a) from two years of the model simulation and (b) from an analysis of 19 years of TPJ data. RMS amplitudes are along the satellite tracks and binned into $1° \times 1°$ squares.

annual zonal mean stratification of the model simulation and the climatological data [*Steele et al.*, 2001] are shown in Figure S1 in the auxiliary material and reveal a well simulated vertically stratified ocean.[1]

[8] The model is explicitly forced by the gravitational forcing of the sun and moon. For each simulated time-step the actual positions of sun and moon are computed by means of the semi-analytic planetary theory VSOP87 [*Bretagnon and Francou*, 1988], and the gravitational forcing of second degree is determined. Thus, hundreds of tidal constituents are implicitly considered in this simulation, including seasonal, annual and nodal cycles. The LSA effect is described by a parameterization for baroclinic models [*Thomas et al.*, 2001].

[9] A detailed description of the effect of the ocean tide forcing on specific properties of the MPI-OM, i.e., on the eddy viscosity, eddy diffusivity, non-linear bottom friction and on the large scale ocean circulation, can be found in *Müller et al.* [2010], where ocean tides have been forced in the coupled atmosphere, land hydrology, and ocean model.

## 3. Evaluation of Barotropic and Baroclinic Tides

[10] In the following, we evaluate the barotropic tide solutions for the eight major diurnal and semi-diurnal constituents by a comparison with the reference data set of 102 pelagic tide measurements [*Shum et al.*, 1997]. The root-mean-square (RMS) values for each tidal constituent show a similar accuracy (Table S1), as those obtained by *Arbic et al.* [2010, Table 3], and consequently the total variance captured (92.8%) is close to that of the Arbic et al. study (92.6%), who used an ocean circulation and tide model with $1/12°$ horizontal resolution. In the model used in the present

---

[1] Auxiliary materials are available in the HTML. doi:10.1029/2012GL053320.

study, we neglect a parameterization of the internal wave drag since we will see in the following that the energy transfer from barotropic to baroclinic tides is simulated by the model. Thus, we would rather need a parameterization for the dissipative processes of baroclinic tidal dynamics, e.g., of turbulent internal wave breaking, which are not resolved by the model. However, as we will see in the next paragraph, the damping of the internal tides is already too high in the model simulation, which is presumably caused by numerical diffusion and the explicitly included biharmonic viscosity.

[11] In order to evaluate the simulated baroclinic tidal pattern, we use an along-track harmonic analysis of 19 years of TOPEX, Poseidon, Jason-1, and Jason-2 (TPJ) altimeter data, as described in *Cherniawsky et al.* [2001] and *Foreman et al.* [2009], while using a total of 26 tidal constituents, which include M_2, and its annual satellites. The along-track M_2 tide from satellite altimeter and from the model simulation are high-pass filtered, with a cutoff wavelength of about 350 km, in order to remove the long-wave barotropic tide signal. The RMS amplitude for each $1° \times 1°$ square in regions of the deep ocean (deeper than 1000 meter) has been computed, and shown in Figure 1. The results from satellite altimeter and model simulation show the same regional hot spots of internal tide generation, where local surface amplitudes of internal waves exceed 20 mm. The internal waves propagate away from the generation sites, though damping in the model is larger than in the observations. Thus, internal wave amplitudes are generally underestimated in the model simulation.

[12] The horizontal resolution of around 10 km allows this model simulation to resolve internal waves with wavelengths longer than about 80 km. Thus, we expect that in the deep ocean only first and possibly second baroclinic modes are resolved [see also *Arbic et al.*, 2010].

[13] The global pattern of the M_2 barotropic to baroclinic tidal energy conversion rate is shown in Figure 2. The conversion rate is estimated from $\left\langle \overline{g\rho'W} \right\rangle$, where $\langle \rangle$ and $^-$ denote averages in time and in the vertical, respectively. W is the barotropic vertical velocity, ρ' is the perturbation density associated with tidal motions, and g the gravitational acceleration [*Kang and Fringer*, 2011]. The global integral amounts to 1.2 TW and is close to values given by previous studies, e.g., 1.1 TW of *Morozov* [1995], 0.7 TW of *Egbert and Ray* [2000], and 0.62 TW of *Simmons et al.* [2004]. As well, a local estimate along the Hawaiian ridge of 14 GW compares reasonably well with previous modeling and observational studies [e.g., *Simmons et al.*, 2004, and references therein].
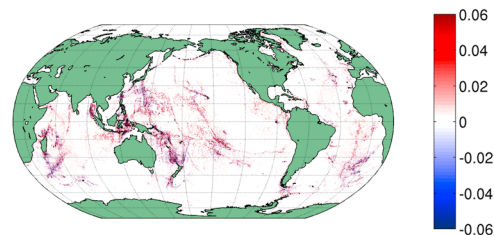
Figure 2. The M_2 barotropic to baroclinic tidal energy conversion is shown in W/m^2. Global sums of positive and negative conversion rates yield 1.7 TW and -0.5 TW, respectively, resulting in a net energy conversion of 1.2 TW.

[14] We conclude that the mode-1 internal tide generation is realistically simulated and that the model will need further adjustment towards a more realistic damping of the internal tides. However, the observed values include contributions from noise and measurement errors of the order of 5–10 mm, so the differences between the model and altimetry derived RMS amplitudes may be less significant.

4. Seasonality of Tides

[15] The seasonal cycle of the M_2 tidal constituent, which is explicitly forced by the gravitational forcing, amounts to only about 0.7% of the M_2 tidal amplitude and is described by its annual satellites α_2 and β_2 [e.g., *Hartmann and Wenzel*, 1995] (also called MA2 and Ma2 [*Corkan*, 1934] or MA2 and MB2 [*International Hydrographic Organization*, 2006]). These two constituents are implicitly considered in the lunisolar tidal potential used in the present study.

[16] The seasonal cycle, which stems from the changing response of the ocean to the tidal forces, can be much larger and affect both barotropic and baroclinic tides. Barotropic tides can be modified by seasonal changes of stratification [*Kang et al.*, 2002; *Müller*, 2012], of sea-ice coverage [*St-Laurent et al.*, 2008], and of meteorological conditions, whereas baroclinic tides are sensitive to stratification and mean flow conditions [*Gerkema et al.*, 2004; *Jan et al.*, 2008].

[17] The seasonal cycle of the M_2 amplitude can be quantified either by a seasonal subsampling of the sea level records, or by using a record longer than one year and estimating the annual satellites of M_2 by a least square method [*Foreman et al.*, 2009]. In the latter case the seasonal cycle is reconstructed by superposing α_2 and β_2 and computing the amplitude and the phase of the seasonal cycle. The analysis of the satellite data has been performed exclusively by the latter method and due to the presence of noise and measurement errors in altimetry data, we used editing criteria as in *Cherniawsky et al.* [2010]. Model data are analysed also by seasonal subsampling, in order to compare results with other observational studies or to overcome limits in storage space. For example, it was not possible to store the three dimensional horizontal velocity fields for one year with a high temporal resolution.

[18] Model-simulated internal tide amplitude differences between winter (November - March) and summer (June - September) are shown in Figure 3a. The seasons are named with respect to the northern hemisphere and the specific time periods have been chosen to correspond with the study of *Ray and Zaron* [2011]. We find that in most areas the seasonality of the internal tides is below 5 mm. However, in some areas, such as western Pacific, around Madagascar, and Bay of Bengal the seasonal difference in the surface internal wave expression can exceed this threshold.

[19] In the following we will focus on the western Pacific, in particular on the region of Yellow, East China, and South China Seas. In the South China Sea the largest seasonal signal in the M_2 internal tide was found by *Ray and Zaron* [2011] along the satellite track which crosses the South China Sea from south-west to north-east and intersects with Taiwan (the track is highlighted by a magenta line in Figure 3c). Along this track the internal tide surface signature obtained from 19 years of satellite altimeter data analysis and of the model simulation in summer and winter are plotted in Figure 3b. There are generally some inconsistencies between

the simulated and observed internal tide. However, the phase offset between the winter and summer simulation, which is also revealed from the observation [*Ray and Zaron*, 2011] is captured. The along-track internal tide in Figure 3b also shows internal waves generated at the model's grid scale and consequently they are not trustworthy. It seems that these small scale fluctuations are only problematic at particular locations, here, e.g., between 19°N and 22°N, and have no effect on our main results, since they are averaged out in one degree bins of Figures 1 and 3a.

[20] The simulated and observed seasonal cycle determined from the α_2 and β_2 tidal constituents is shown in Figure 3c. There is a pronounced seasonal cycle in the Yellow Sea and East China Sea, captured by both model and satellite altimeter. This feature is consistent with the study of *Kang et al.* [2002] and is presumably caused by the effect of the seasonally varying stratification on barotropic tides [*Müller*, 2012]. In the South China Sea, a seasonality in the low mode internal wave structure is presented in the model simulation. Furthermore, the altimeter data analysis shows seasonal variations exceeding 20 mm, which might also be caused by perturbations in the internal tides.

[21] The largest seasonal phase differences along the displayed satellite track are in the model simulation and in the *Ray and Zaron* [2011] study at about 17°N. A vertical section is chosen such that it connects the generation site in Luzon Strait with the largest observed differences along the satellite track. This section is highlighted in Figure 3c. Obviously, the simulated seasonal amplitude shown in the latter figure reveals an internal tide propagating westwards along this section with high seasonal variability. Vertical density structure, M_2 baroclinic velocity, and the high-pass filtered surface tide along this section are shown in Figure 4. In summer, a seasonal thermocline develops, which is located at approximately 50–100 meter depth. This thermocline disappears in winter, when only the deeper permanent pycnocline exists. These seasonal changes in stratification have a considerable effect on the magnitude of the baroclinic tidal currents in the upper layer (Figures 4a and 4b) and on the propagation speed of the internal tide (Figure 4c). The increased baroclinic velocities above the seasonal thermocline are consistent with the study of *Gerkema et al.* [2004], in which the seasonality of the internal tide in the Bay of Biscay is analysed. They attributed this effect to an internal tide, which is generated in summer above the seasonal thermocline. Seasonal changes in phase speed of the internal tide in the South China Sea, were also shown by *Jan et al.* [2008]. They consistently found faster internal tides propagating into the South China Sea in summer.

[22] These results emphasize the role of changing stratification conditions at the generation site and along the propagation path of the internal tides. Seasonal changes in the monsoon forcing substantially change the pathways of the Kuroshio in this region and thus induce inter-annual changes in the density structure. In particular, observations show that this seasonally varying wind forcing impacts the penetration depth of the Kuroshio into the South China Sea through Luzon Strait [*Rudnick et al.*, 2011], which is consistently captured by the model simulation (Figure S2).

5. Summary and Conclusion

[23] In the present study we introduce a high resolution ocean circulation and tide model with a stationary seasonal

(a) seasonal difference surface internal tide

## (b) along-track internal tide

(c) seasonal tidal amplitude
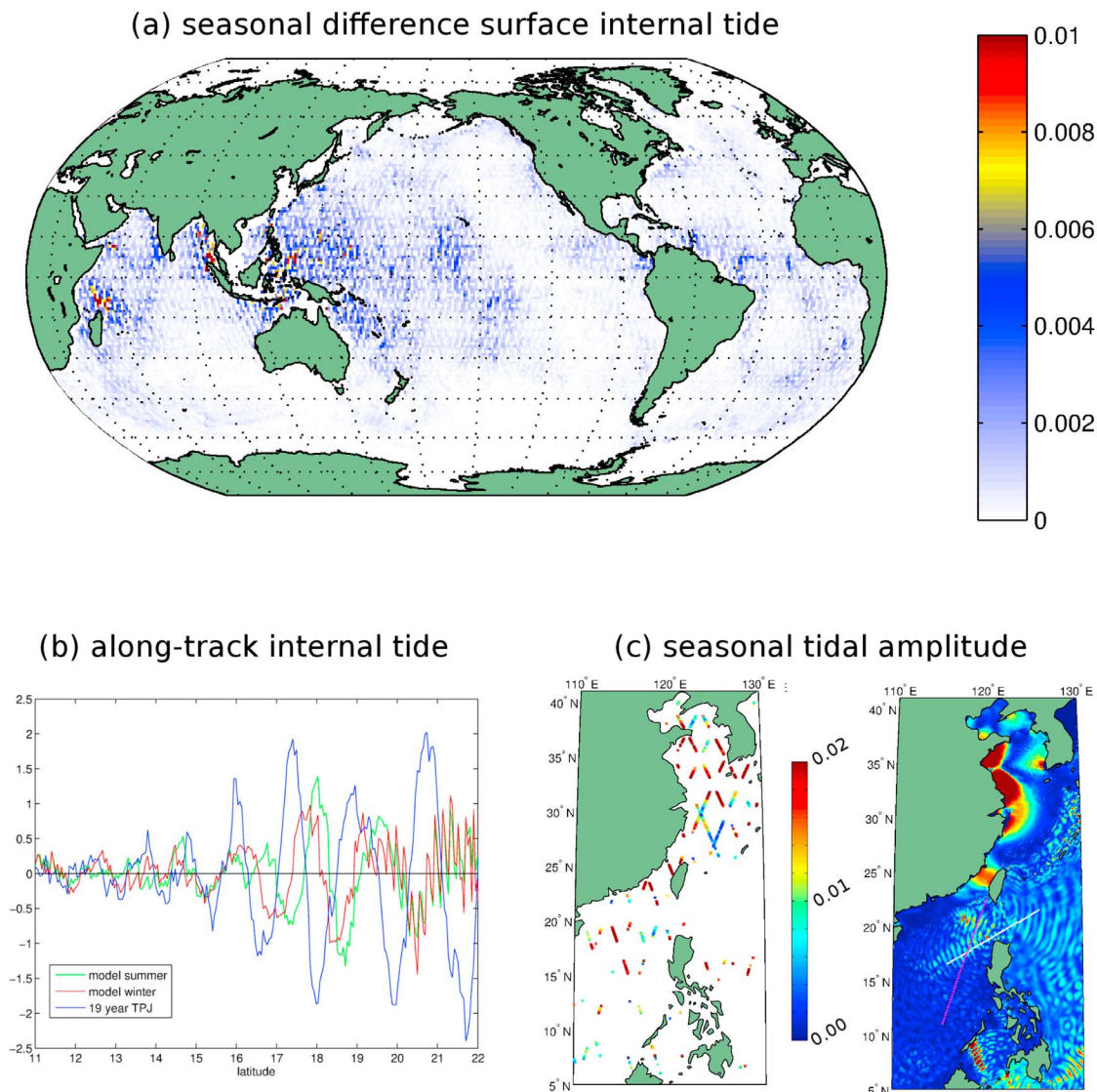
Figure 3. (a) The RMS difference (in meter) of the model-simulated internal tide amplitude differences between winter (November - March) and summer (June - September) are shown. The satellite tracks of Figure 1 are used and each point is binned into $1° \times 1°$ squares. (b) The M_2 internal tide (high-pass filtered along-track tidal amplitude in cm) along a particular track in the South China Sea. (c) The seasonal amplitude (in meter) is derived from the annual satellites of M_2 (left) in altimetry data and (right) in the model simulation. In Figure 3c (right) the satellite track used for Figure 3b and the model section for Figure 4 are highlighted by magenta and white lines, respectively.

cycle, forced by climatological wind stress, heat and fresh-water fluxes. The ocean tides are forced by a full lunisolar astronomical forcing. The simulation explicitly resolves the eddying ocean circulation and the barotropic and low mode baroclinic tides. The accuracy of the barotropic tide is comparable with recent forward tide models which are not constrained by satellite data [*Arbic et al.*, 2004; *Griffiths and Peltier*, 2009; *Arbic et al.*, 2010]. In this simulation the barotropic to baroclinic tidal energy conversion rate is 1.2 TW. The simulated internal tide field compares reasonably well with the global map derived from satellite altimeter data. However, the model tends to overestimate the damping

of the internal tides, which invites further research and improvement.

[24] An important feature of this modeling approach is that the ocean tide forcing implicitly contains all tidal constituents of second degree and simulates the interannual variability of barotropic and baroclinic tides. Our model is able to predict regions where seasonal, or more generally non-stationary variations of tides can be expected. As an example, the seasonality of the internal tides in the South China Sea is discussed and agrees with satellite altimeter data [*Ray and Zaron*, 2011]. The model results are consistent, and reveal the effect of seasonally varying stratification, controlled by
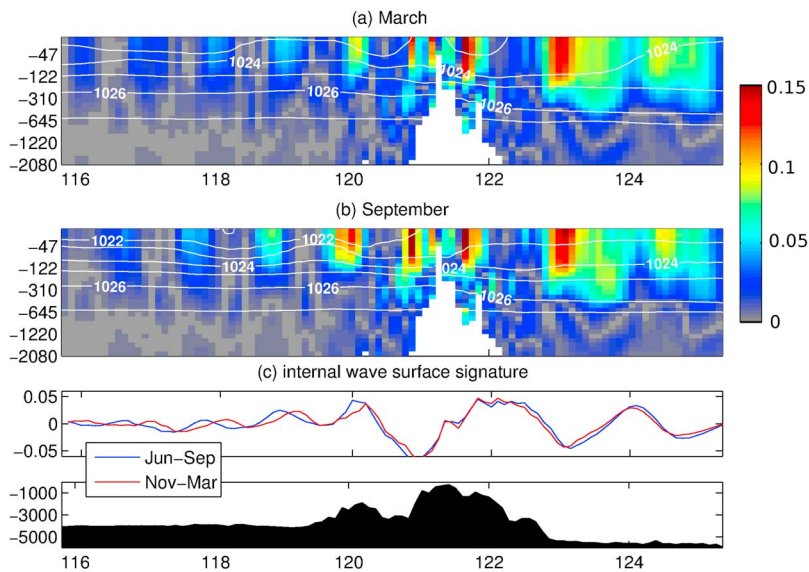
Figure 4. Vertical view of the section highlighted in Figure 3c. (a and b) The zonal baroclinic M$_2$ tidal velocity (m/s) in the upper 2080 meters during March and September, with potential density (kg/m3) shown using white contour lines. Note that the vertical spacing of the model layers is non-linear. (c) High-pass filtered surface tide during winter and summer (these seasons are defined as in Figure 3) and depth relief along this section. Y-axis units are metres and the x-axis is longitude (degrees East).

seasonal solar radiation and wind forced circulation, on the propagation of the internal tide. These results emphasize the use of global eddy-resolving ocean circulation and tide models to further understand the complex interplay between the generation and propagation of the internal tides and the low frequency ocean circulation.

References

Arbic, B. K., S. T. Garner, R. W. Hallberg, and H. L. Simmons (2004), The accuracy of surface elevations in forward global barotropic and baroclinic tide models, *Deep Sea Res., Part II*, *51*, 3069–3101.

Arbic, B. K., A. J. Wallcraft, and E. J. Metzger (2010), Concurrent simulation of the eddying general circulation and tides in a global ocean model, *Ocean Modell.*, *32*, 175–187.

Arbic, B. K., J. G. Richman, J. F. Shriver, P. G. Timko, E. J. Metzger, and A. J. Wallcraft (2012), Global modeling of internal tides within an eddying ocean general circulation model, *Oceanography*, *25*, 20–29.

Bretagnon, P., and G. Francou (1988), Planetary theories in rectangular and spherical variables—VSOP 87 solutions, *Astron. Astrophys.*, *202*, 309–315.

Cherniawsky, J., and G. Holloway (1991), An upper-ocean general circulation model for the North Pacific: Preliminary experiment, *Atmos. Ocean*, *29*, 737–784.

Cherniawsky, J. Y., M. G. G. Foreman, W. R. Crawford, and R. F. Henry (2001), Ocean tides from TOPEX/POSEIDON sea level data, *J. Atmos. Oceanic Technol.*, *18*, 649–664.

Cherniawsky, J. Y., M. G. G. Foreman, S. K. Kang, R. Scharroo, and A. J. Eert (2010), 18.6-year lunar nodal tides from altimeter data, *Cont. Shelf Res.*, *30*, 575–587.

Corkan, R. H. (1934), An annual perturbation in the range of tide, *Proc. R. Soc. London, Ser. A*, *144*, 537–559.

Egbert, G., and R. D. Ray (2000), Significant dissipation of tidal energy in the deep ocean inferred from satellite altimeter data, *Nature*, *405*, 775–778.

Foreman, M. G. G., J. Y. Cherniawsky, and V. A. Ballantyne (2009), Versatile harmonic tidal analysis: Improvements and applications, *J. Atmos. Oceanic Technol.*, *26*, 806–817.

Gerkema, T., F.-P. A. Lam, and L. R. M. Maas (2004), Internal tides in the Bay of Biscay: Conversion rates and seasonal effects, *Deep Sea Res., Part II*, *51*, 2995–3008.

Griffiths, S. D., and W. R. Peltier (2009), Modeling of polar ocean tides at the Last Glacial Maximum: Amplification, sensitivity, and climatological implications, *J. Clim.*, *22*, 2905–2924.

Hartmann, T., and H. Wenzel (1995), The HW95 tidal potential catalogue, *Geophys. Res. Lett.*, *22*(24), 3553–3556.

International Hydrographic Organization (2006), *Harmonic Constants: Product Specification*, 1st ed., Monaco.

Jan, S., R. Lien, and C.-H. Ting (2008), Numerical study of baroclinic tides in Luzon Strait, *J. Oceanogr.*, *64*, 789–802.

Jungclaus, J., M. Botzet, H. Haak, N. Keenlyside, J. J. Luo, M. Latif, J. Marotzke, U. Mikolajewicz, and E. Roeckner (2006), Ocean circulation and tropical variability in the coupled model ECHAM5/MPI-OM, *J. Clim.*, *19*, 3952–3972.

Kang, D., and O. B. Fringer (2011), Energetics of barotropic and baroclinic tides in the Monterey Bay area, *J. Phys. Oceanogr.*, *42*, 272–290.

Kang, S. K., M. G. G. Foreman, H.-J. Lie, J.-H. Lee, J. Cherniawsky, and K.-D. Yum (2002), Two-layer tidal modeling of the Yellow and East China Seas with application to seasonal variability of the M$_2$ tide, *J. Geophys. Res.*, *107*(C3), 3020, doi:10.1029/2001JC000838.

Morozov, E. (1995), Semidiurnal internal wave global field, *Deep Sea Res., Part I*, *42*, 135–148.

Müller, M. (2012), The influence of changing stratification conditions on barotropic tidal transport and its implications for seasonal and secular changes of tides, *Cont. Shelf Res.*, doi:10.1016/j.csr.2012.07.003, in press.

Müller, M., H. Haak, J. H. Jungclaus, and J. Sündermann (2010), The effect of ocean tides on a climate model simulation, *Ocean Modell.*, *35*, 304–313.

Ray, R. D., and G. T. Mitchum (1997), Surface manifestation of internal tides in the deep ocean: Observations from altimetry and island gauges, *Prog. Oceanogr.*, *40*, 135–162.

Ray, R. D., and E. D. Zaron (2011), Non-stationary internal tides observed with satellite altimetry, *Geophys. Res. Lett.*, *38*, L17609, doi:10.1029/2011GL048617.

Rudnick, D. L., et al. (2011), Seasonal and mesoscale variability of the Kuroshio near its origin, *Oceanography*, *24*, 52–63.

Shum, C. K., et al. (1997), Accuracy assessment of recent ocean tide models, *J. Geophys. Res.*, *102*, 25,173–25,194.

Simmons, H. L., R. H. Hallberg, and B. K. Arbic (2004), Internal wave generation in a global baroclinic tide model, *Deep Sea Res., Part II*, *51*, 3043–3068.

Steele, M., R. Morley, and W. Ermold (2001), A global ocean hydrography with a high quality Arctic Ocean, *J. Clim.*, *14*, 2079–2087.

St-Laurent, P., F. J. Saucier, and J.-F. Dumais (2008), On the modification of tides in a seasonally ice-covered sea, *J. Geophys. Res.*, *113*, C11014, doi:10.1029/2007JC004614.

Thomas, M., J. Sündermann, and E. Maier-Reimer (2001), Consideration of ocean tides in an OGCM and impacts on subseasonal to decadal polar motion excitation, *Geophys. Res. Lett.*, *28*, 2457–2460.